

# Resolving Morphology and Antibody Labeling Over Large Distances in Tissue Sections

MARC D. JACOBS, PAUL J. DONALDSON, MARK B. CANNELL, AND CHRISTIAN SOELLER\*

*Department of Physiology, School of Medical and Health Sciences, The University of Auckland, Auckland, New Zealand*

**KEY WORDS** two-photon microscopy; image processing; cell morphology; gap junctions; connexin; eye lens

**ABSTRACT** Protein expression patterns are a primary determinant of tissue function and in this study we developed methods to study protein expression over macroscopic distances at subcellular levels of detail. Using the mammalian lens as a model tissue system, we show that by combining two-photon microscopy with novel image montage methods (fast beam blanking coupled with mathematical alignment tools) we have extended the limited field of view of laser scanning microscopes. To illustrate the utility of our approach, the distribution of connexin-46 was visualized across equatorial sections of the rat mammalian lens. By optimizing fixation protocols, good morphological preservation could be achieved over the thickness of the lens (~4 mm) while preserving antigenicity of lens proteins. Using the same image data, changes in lens fiber cell morphology were mapped quantitatively by automatic image analysis routines. The methods presented should be generally applicable to any tissue system where changes in antibody labeling and tissue structure occur over large and small distances. *Microsc. Res. Tech.* 62:83–91, 2003. © 2003 Wiley-Liss, Inc.

## INTRODUCTION

Confocal laser-scanning microscopy (CLSM) has become the method of choice to investigate the spatial distribution of fluorescently labeled molecules and structures in biological samples with high spatial resolution. The principal advantage of CLSM compared to conventional wide-field fluorescence microscopy resides in its ability to reject light emitted above or below the focal plane (Inoue, 1995). Two-photon microscopy (TPM; Denk et al., 1995) provides an alternative to CLSM and can achieve similar spatial resolution without the need for a confocal pinhole. Since the excitation in TPM is confined to the focal volume, no photobleaching occurs outside of the region actually being imaged (Cannell and Soeller, 1997). Furthermore, when imaging multilabeled specimens longitudinal chromatic aberrations can be eliminated (Wan et al., 1999) and it is possible to image deeper into strongly scattering tissues (as compared to CLSM, see Soeller and Cannell, 1999; Xu et al., 1996).

The high spatial resolution provided by both CLSM and TPM is usually used to image the distribution of small, subcellular structures within small tissue samples. However, variations in the distribution of various molecules may also occur over wide distances as the tissue of interest may compartment function in different zones. Thus, to obtain a clear picture of the role of a particular molecule in tissue function we need to examine the distribution of that molecule at the cellular and subcellular level as well as how the distribution varies across the tissue. In order to combine the high spatial resolution provided by CLSM and TPM with an extended field of view, several overlapping image volumes must be combined to cover a field that is much larger than that of the microscope (Beck et al., 2000; Becker et al., 1996). The combination of fields of view requires fast, accurate, and seamless joining of images,

especially if quantitative analysis is to be performed on the composite image.

The eye lens is composed of many thousands of densely packed fiber cells whose morphological arrangement is critical to its high optical transparency. The importance of cell structure to lens function is emphasized by the observation that a variety of pharmacological and genetic disturbances cause distortion of the regular fiber cell array, resulting in loss of lens transparency and ultimately cataract (Young et al., 2000; Lichtstein et al., 1999; Gong et al., 1997; White et al., 1998). The anterior half of the lens is covered by a monolayer of cuboidal epithelium (Zampighi et al., 2000). Throughout life, epithelial cells differentiate to form fiber cells at the equator by elongating and becoming enveloped by younger fiber cells. Differentiation continues as fiber cells are compacted deeper in the lens and as the cells age cell morphology undergoes significant change. Being avascular, the lens is thought to generate an endogenous "microcirculation" that enables homeostasis and thus maintains tissue transparency (Donaldson et al., 2001). While previous qualitative studies have shown that cell morphology varies within the lens (e.g., Bassnett, 1995), understanding the relevance of these morphological changes to homeostatic mechanisms requires quantification throughout the lens.

\*Correspondence to: Dr. Christian Soeller, Department of Physiology, School of Medical and Health Sciences, The University of Auckland, 85 Park Rd., Grafton, Auckland 1, New Zealand. E-mail: c.soeller@auckland.ac.nz

Received 8 November 2002; accepted in revised form 27 March 2003

Contract grant sponsors: the University of Auckland Research Committee, the Marsden Fund of New Zealand and the Wellcome Trust (UK).

DOI 10.1002/jemt.10360

Published online in Wiley InterScience (www.interscience.wiley.com).

Here we report a set of techniques and image processing algorithms that we have developed for quantitative whole-lens mapping of morphology with subcellular resolution. The methods we present should be generally applicable to any tissue system where changes in antibody labeling occur over large and small distances. We present data which show changes in morphology and a cell junctional protein (connexin-46) across hundreds of cell layers within the adult mammalian lens, illustrating the utility of our methods.

## MATERIALS AND METHODS

### Tissue Sectioning

Twenty-one-day-old Wistar rats were killed by CO<sub>2</sub> asphyxiation in accordance with protocols approved by the University of Auckland Animal Ethics Committee. Lenses were dissected in phosphate-buffered saline (PBS) and fixed in 0.75% w/v paraformaldehyde in PBS for 24 hours at room temperature. Lenses were then washed 3 × 10 minutes in PBS followed by cryoprotection in 10% w/v sucrose for 1 hour at room temperature, then 20% sucrose and finally 30% sucrose at 4°C overnight (all in PBS). Fixed lenses were mounted in Tissue-Tek O.C.T. compound (Sakura Finetechnical Co., Tokyo, Japan) at 4°C on prechilled chucks. Chucks were immersed in liquid nitrogen for 25 seconds, then stored on dry ice. Using disposable blades, 10 μm sections were cut (S-35, Feather Safety Razor Co., Japan) at -18°C on a cryostat (CM3050, Leica, Germany) and placed onto slides coated with poly-L-lysine. Slides were then washed 4 × 5 minutes in PBS. Unless otherwise stated, all chemicals were obtained from Sigma Aldrich (New Zealand).

### Fluorescent Labeling

All incubations were carried out either at room temperature for the times indicated or at 4°C overnight in a humidified box. Slides were treated for 1 hour with blocking solution (3% w/v bovine serum albumin, 3% v/v fetal calf serum in PBS), washed 3 × 5 minutes in PBS, and treated for 2 hours with rabbit antirat connexin-46 (Cx46) antibody (Alpha Diagnostic International, San Antonio, TX) diluted 1:200 in blocking solution. This antibody labels large gap junctions between fiber cells (Jacobs et al., 2001) and complements the general membrane label used elsewhere on the cell surface (see below). Slides were washed 3 × 5 minutes in PBS and treated for 1.5 hours in the dark with goat antirabbit Alexa Fluor 488 secondary antibody (Molecular Probes, Eugene, OR) diluted 1:200 in blocking solution. After washing 3 × 5 minutes in PBS, slides were labeled for 1.5 hours in the dark with Alexa Fluor 350-conjugated wheat germ agglutinin (WGA; Molecular Probes) diluted to 40 μg/ml in PBS. The lectin WGA labels glycosylated membrane proteins and provided a general marker of fiber cell membranes (e.g., Bond et al., 1996). Finally, after washing 3 × 5 minutes in PBS, slides were mounted in 10 μl Citifluor AF1 (Citifluor, Leicester, UK) and stored at 4°C.

### Two-Photon Microscopy

Excitation for TPM was provided by a mode-locked Ti:Sapphire laser (Coherent, Santa Clara, CA) that was coupled to a modified confocal microscope (LSM 410, Zeiss, Jena, Germany) (Soeller and Cannell,

1996). The laser was tuned to a center wavelength of ~755 nm to simultaneously excite both labels. Slides were imaged using a 40× 1.2 NA water immersion objective. The main dichroic filter separating illumination and emission wavelength from each other was a short pass filter with an edge centered at 650 nm (Chroma Technology, Brattleboro, VT). Emitted light was collected from both fluorescent labels simultaneously with all emission pinholes fully open (see also Konig, 2000; So et al., 2000). The emitted light was split into the two channels by a long pass filter centered at 495 nm (495DRLP, Omega Optical, Brattleboro, VT). Emission bandpass filters centered at 450 nm (450DF65, bandwidth 65nm, Omega Optical) and 535 nm (HQ535/50, bandwidth 50 nm, Chroma Technology) were used to select the signals from Alexa Fluor 350 and Alexa Fluor 488, respectively. Image stacks were collected at a sampling resolution of ~200 nm in plane and 300 nm along the optical axis. To extend the total field of view a number of overlapping 1024 × 1024 × 30 pixel image stacks were acquired such that a total volume of ~750 × 385 × 10 μm was covered. The positioning and extent of overlap of the image stacks were electronically controlled and recorded using a motorized stage of ~1 μm position accuracy (Zeiss, Jena, Germany). To eliminate photobleaching during the retrace of the raster scanning beam between image lines, a custom-built electronic switching mechanism was coupled to a Pockels cell (model 350-50, Conoptics, Danbury, CT) for fast intensity modulation of the beam (Soeller and Cannell, 1999). Briefly, the custom electronics consisted of a set of digital counters that were fed from the pixel clock and line start signals generated by the LSM 410 scanning electronics. By preloading the counters, the electronics were able to produce a pulse which was valid over the image region selected by the user (set using thumbwheel switches to define start x-y coordinate and size of the region of interest). This pulse was shaped and passed to the video input of the Pockels cell controller. The Pockels Cell (contrast ratio 500:1 at 633 nm) therefore acted as a fast electro-optical shutter. The pulse broadening caused by the Pockels cell was small (e.g., a 120 fs pulse was broadened to ~140 fs) and could be fully compensated for by a prism compressor. Note that alternative acousto-optical modulators are more dispersive (leading to significant pulse broadening) and also introduce a spatial pulse chirp which makes them generally unacceptable as a laser switch for femtosecond pulses (although see Lechleiter et al., 2002). Scanned images were written directly to hard disk for off-line analysis and archived on recordable CDs. Image processing and analysis were performed using custom routines written in the IDL programming language (Research Systems, Boulder, CO) running on Silicon Graphics Workstations.

## RESULTS

### Lens Sectioning

Densely packed fiber cells can be seen in transverse section in equatorial sections of the lens (Fig. 1A). In order to examine cell morphology and preserve antigenicity of proteins, it was necessary to develop specific fixation protocols. Published protocols, involving fresh 2–4% paraformaldehyde treatment for 1–3 hours, re-

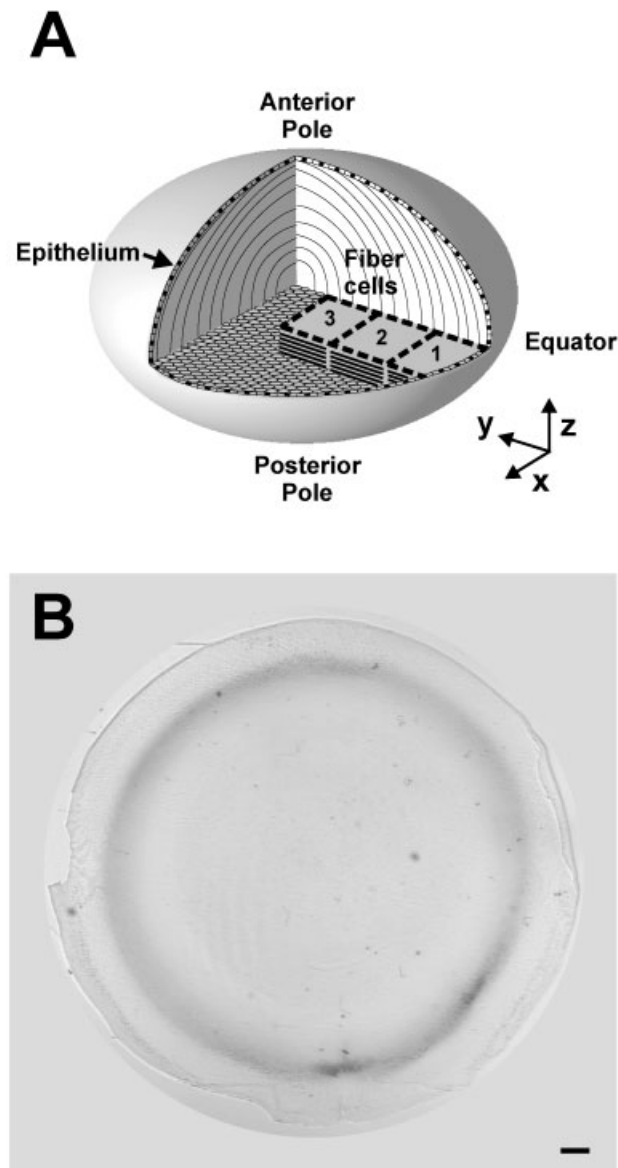


Fig. 1. Equatorial sections of the rat lens. **A:** Schematic of lens morphology illustrating fiber cell geometry in equatorial sections. Positions of image stacks collected by TPM at the equator are also indicated. **B:** Low-magnification brightfield image of an equatorial lens section. Note that the section is smooth throughout the lens, including the dense core region. Scale bar = 200  $\mu\text{m}$ .

sulted in sections that retained good morphology and antibody labeling only in the periphery (not shown). We therefore reduced the paraformaldehyde concentrations to 0.5–2% while extending the fixation time to 16–48 hours (at room temperature). In addition, effects of varying section thickness (5–50  $\mu\text{m}$ ) and cryosectioning temperature ( $-10^{\circ}\text{C}$  to  $-30^{\circ}\text{C}$ ) were evaluated. A systematic assessment of sections showed that an optimal balance between good morphology and good antibody signal was obtained using 0.75% paraformaldehyde for 24 hours. The relatively low concentration of fixative did not significantly change lens dimensions (<3%, data not shown). Furthermore, 10- $\mu\text{m}$  sections

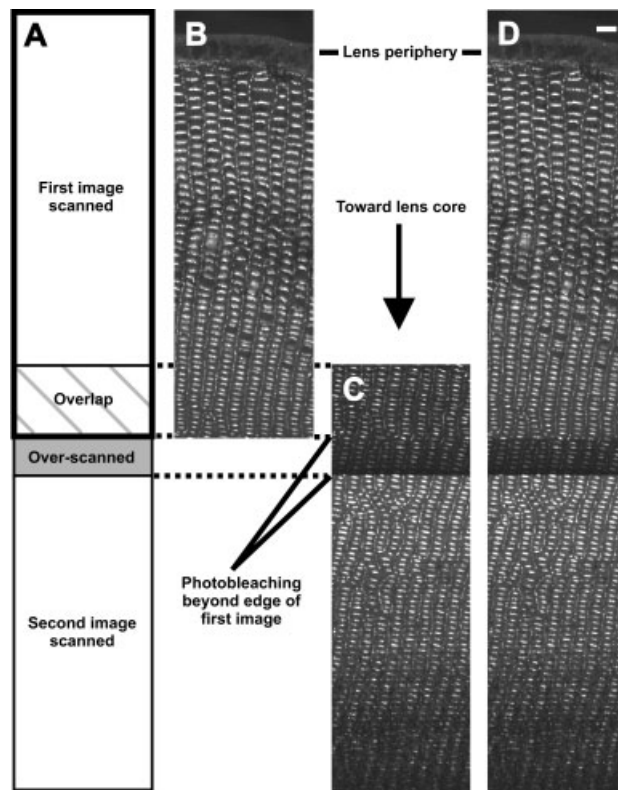


Fig. 2. Example of photobleaching due to overscanning. **A:** Diagram of two overlapping images collected consecutively along an equatorial lens radius, showing photobleaching in the area of overlap and also in an over-scanned area beyond the edge of the first image. While the first image is unaffected (**B**), the second image shows photobleaching in the area over-scanned when the first image was collected (**C**). As a result, the montage of both images exhibits a photobleached region that prevents the collection of a seamless dataset (**D**). Scale bar = 10  $\mu\text{m}$ .

cut at  $-18^{\circ}\text{C}$  were smooth to the lens center most often within the tested range of parameters (Fig. 1B).

### Imaging of Overlapping Regions

Equatorial sections showing good morphological preservation were labeled with WGA (a cell membrane marker) and antibodies against Cx46 (to label gap junction plaques) and imaged by TPM. A number of image stacks covering the thickness of the section were collected along a radius into the lens starting at the periphery (Fig. 1A). Adjacent image stacks were positioned so as to overlap one another in the  $x$ ,  $y$ , and  $z$  planes. In this way two contiguous columns of image stacks along a radius were recorded, which overlapped one another by a fixed amount in the  $x$ - $y$  plane and by a variable amount along the  $z$ -axis (the variability being due to small variations in section flatness after mounting on the coverslip). Assembling a composite image from such image stacks is complicated by photobleaching of the fluorescent markers. This problem is demonstrated in Figure 2, which shows representative images from two adjacent, overlapping image stacks. Due to the mechanical inertia of the galvanometric scan mirrors the laser beam will generally slow down

before reversing direction and moving back through the imaged region. Most commercial microscopes effectively limit the data acquisition to the central portion of the scan during which the beam moves with approximately uniform velocity. As a result, there are over-scanned regions beyond the image edges (Fig. 2A) which receive an increased light dosage due to the slow beam passage. While this did not affect the first image (Fig. 2B), it affected an area in the field of view of the second image (Fig. 2C) *before* it could be acquired in the second stack. Therefore, after combining the two stacks, a dark band remained in the area corresponding to the overscanned region (Fig. 2D). Such overscanning precludes the generation of a seamless composite image. To avoid this problem, we constructed a fast electro-optic shutter which limited preparation exposure to the period of data acquisition within the field of view. This device was synchronized to the pixel clock signals derived from the scan control hardware within the LSM 410 (see Materials and Methods).

### Alignment and Assembly of Images

To construct a montage of adjacent image stacks in the  $x$ - $y$  plane, an extended focus image was generated (by maximum projection; e.g., Beck et al., 2000) from each image stack. This use of extended focus images ensured that appropriate data were used from each image stack despite small changes in  $z$ -intervals spanned by different stacks. (Note that for thicker sections, parts of the image stacks may be selected for construction of extended focus images for registration purposes.) Figure 3A shows the arrangement of the overlapping eight image stacks in the  $x$ - $y$  plane overlaid onto the resulting composite extended focus image. Approximate horizontal alignment of stacks to within  $\sim 1 \mu\text{m}$  was possible from coordinates provided by the motorized stage. However, since the  $x$ - $y$  sampling resolution was significantly higher ( $\sim 200 \text{ nm}$  per pixel in-plane) than the accuracy of the motorized stage, seamless alignment of overlapping images required more accurate registration. To achieve this, we employed a cross-correlation technique (e.g., Milgram, 1975; Dani and Chaudhuri, 1995; Beck et al., 2000; Becker et al., 1996; Milgram, 1975; Ott, 1997) and exploited the known constraints from the motorized stage coordinates to minimize computational cost. Approximately  $20 \mu\text{m}$ -wide data strips in the region of overlap were extracted from each pair of overlapping extended focus images and cross-correlations were calculated for relative shifts of up to  $\pm 1 \mu\text{m}$  ( $\pm 5$  pixels) in  $x$  and  $y$ . Normalized cross-correlations were calculated according to Eq. (1) in Dani and Chaudhuri (1995), where the summation for a given shift in  $x$  and  $y$  was restricted to the region of overlap between data strips. This procedure resulted in a two-dimensional cross-correlation distribution, shown as a surface plot in Figure 3B. Its maximum corresponds to the optimal alignment of the extracted image strips and, therefore, the optimal  $x$ - $y$  alignment of the two stacks. It should be noted that using a normalized correlation technique has the additional benefit that the cross-correlation is insensitive to changes in image contrast between image stacks (Dani and Chaudhuri, 1995). This allowed us to adjust the detector gain settings for each stack to

match the full dynamic range of the 8 bit analog-to-digital conversion.

The localized cross-correlation algorithm consistently yielded a unique optimum  $x$ - $y$  shift, corresponding to a spatial accuracy of  $< 200 \text{ nm}$ . The accuracy was maintained throughout the assembly of a composite image that extended over  $0.75 \text{ mm}$  (Fig. 3A). Once aligned, the intensities of image stacks were adjusted for changes in gain (photomultiplier tube voltage) used during acquisition. This was achieved by referring to a calibration curve that tabulated detector gain versus nominal software gain settings (which had been recorded for each stack). To demonstrate the ability of our approach to seamlessly combine image stacks, Figure 3C shows an enlarged detail of a region where two stacks were combined/aligned. Note that by restricting the period of laser illumination to only the region digitized, bleaching is avoided outside the region of interest.

Following alignment in-plane, a similar strategy was used for accurate alignment of stacks along the optical axis. Two stacks aligned in this way are shown along the  $x$ - $z$  plane in Figure 3D.

### Quantification of Cell Morphology

The range of spatial scales that can be explored from such spatially extended datasets is illustrated in Figure 4. Figure 4A–C shows three regions (extracted from the composite extended focus image, see Fig. 3A), where the display magnification increases 5-fold between images. The images show the cell membrane and gap junction morphology at the tissue, cellular, and subcellular scales, respectively. The maximum resolution of the raw dataset is visible in Figure 4C, where individual pixels measuring  $\sim 200 \times 200 \text{ nm}$  are well defined. On this scale the details of cell shape and the subcellular distribution of gap junction plaques (red) in the cell membrane (green) can be clearly identified. The high resolution available in the composite data makes it possible to study the change in the expression pattern of Cx46 across the lens. Close to the periphery (Fig. 4C), Cx46 is found in broad side plaques and in smaller spots on the narrow sides of fiber cells (where they couple adjacent rows of cells). Deeper in the lens, Cx46 is less clearly organized (Fig. 4D,  $500 \mu\text{m}$  from the periphery) and at a depth of  $\sim 700 \mu\text{m}$  the remaining Cx46 is almost uniformly distributed in the cell membrane (Fig. 4E).

The composite extended focus dataset can be used for quantification of morphological features. Quantification of cell morphology was achieved by digitally identifying and measuring cells in two independent ways (Fig. 5). The first, fully automatic method distinguished between fiber cell membrane and cytosol (Fig. 5A) by calculating a bi-level mask using adaptive thresholding where the mean value of brightness in a  $32 \times 32$  neighborhood of a pixel was used as a local threshold (Fig. 5B). The resulting bi-level image of cell boundaries was then “thinned” to generate a one-pixel-wide “skeleton” (Kong and Rosenfeld, 1989) of cell outlines (Fig. 5C) which were used for automated measurement of cell cross-sectional area and perimeter. Using standard connected component labeling techniques (Kong and Rosenfeld, 1989), cross-sectional areas were determined by automatically measuring the

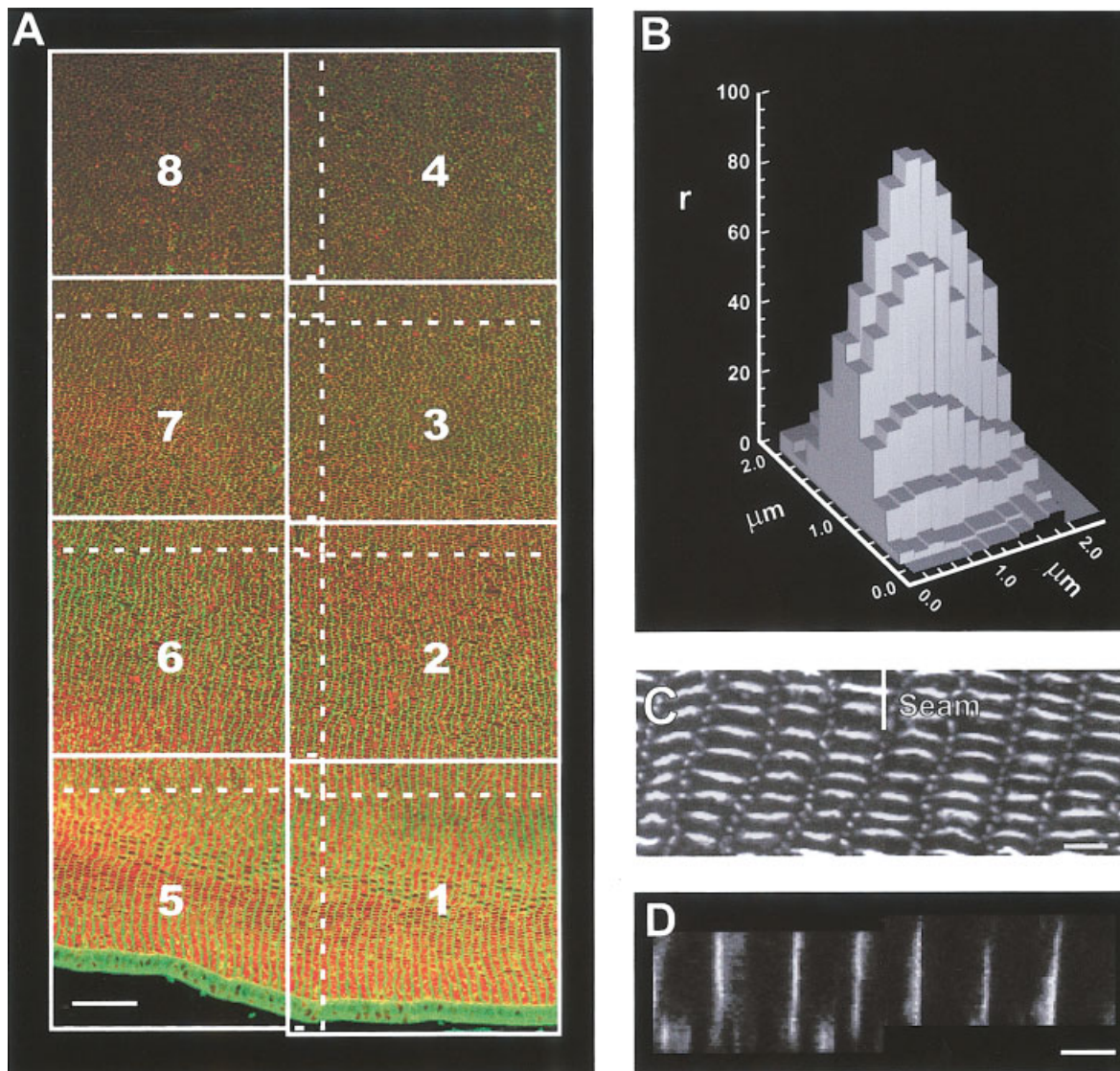


Fig. 3. Aligning overlapping images by correlation. **A:** A set of eight overlapping  $1000 \times 1000$  pixel high-resolution images were aligned to produce one continuous image spanning  $>700 \mu\text{m}$ . Images were joined at solid lines; dotted lines indicate overlapped image borders. Connexin labeling is shown in red, cell membrane labeling (WGA) in green. Scale bar =  $50 \mu\text{m}$ . **B:** Example of a "correlation surface" showing a maximum correlation value  $r$  at the optimal alignment between two overlapping images (the two lower axes represent

translation in the  $x$ - $y$  plane). Each column represents a different pixel alignment between the two images; column height indicates the extent of correlation (expressed as a percentage). **C:** High-magnification view of the seam between images 1 and 5 shown in (A). Scale bar =  $5 \mu\text{m}$ . **D:** The seam between images 1 and 5 viewed at high magnification in the  $x$ - $z$  plane, following correlation along the optical axis. Scale bar =  $5 \mu\text{m}$ . [Color figure can be viewed in the online issue, which is available at [www.interscience.wiley.com](http://www.interscience.wiley.com).]

size of connected background regions (corresponding to the cross-sectional area of individual cells). The cell perimeters were computed by digitally measuring the length of the thinned cell outlines. To verify the automated morphological analysis a second, operator-assisted quantification was performed. Using an interactive program, the operator traced a number of individual cell outlines within a small region of the composite image (Fig. 5D). Once a cell outline was completed, the length of the traced polygon and the area enclosed by that polygon were calculated (Fig. 5E) using standard computer graphics algorithms (Russ, 1995).

Using the image data shown in Figure 3A, these two approaches were used to produce estimates of cell pe-

rimeter and cross-sectional area over a radius of  $700 \mu\text{m}$  sampled in  $20\text{-}\mu\text{m}$  intervals. Figure 6A shows the cell perimeter as a function of distance from the periphery. The values calculated with the fully automatic algorithm agree well with those determined with the semiautomatic procedure. Note that the error bars on values calculated with the semiautomatic procedure are comparatively larger, as only five cells were sampled per interval interactively while  $>100$  cells per data point were sampled with the fully automatic algorithm. Similar quantitative agreement was observed for the cross-sectional measurements shown in Figure 6B. In general, these data show that fiber cell perimeter was relatively constant while cross-sectional area

increased slightly from the lens periphery to a distance of some 700  $\mu\text{m}$  deep at the lens equator (although a slight decrease in cross-sectional area was observed near the lens periphery). Visual inspection suggested that the shape of fiber cells changed from the hexagonal pattern at the periphery progressively to a less

regular and more rounded shape deeper in the lens (Fig. 6C). This impression was confirmed when the perimeter and cross-section data were combined to calculate a unitless form factor as an index of cell circularity (e.g., Russ, 1995):

$$FF = 4\pi * \text{Area} / \text{Perimeter}^2 \quad (1)$$

In this equation, a value of 1 implies a perfect circle and a value of 0 corresponds to a straight line. As shown in Figure 6D, this form factor increased steadily with depth into the lens, rising from  $\sim 0.4$  at the periphery to  $\sim 0.8$  at a depth of 700  $\mu\text{m}$ . These data confirm the impression of a progressive change in cell shape, in agreement with images that were presented previously (but not analyzed, e.g., Bassnett, 1995).

## DISCUSSION

In this study we have quantified lens fiber cell morphology as a continuous function of distance deep into the adult mammalian lens. We developed a fixation and cryosectioning protocol that preserved fiber cell morphology and epitopes to antibodies against major fiber cell proteins throughout the lens. Using this protocol we were able to routinely produce large, high-quality sections whose position and orientation can be accurately chosen with respect to the whole organ. Large image datasets suitable for quantitative analysis covering an extended field of view were recorded at high resolution using a motorized stage and custom-written software for precise image montage. In the presence of photobleaching the use of an electro-optic shutter was crucial to limit photobleaching to the region of data actually acquired. Without limiting photobleaching in this way it would have been impossible to obtain a seamless montage. Quantitative analysis of lens fiber cell morphology showed that fiber cell shape changes as a function of lens radius.

### Preparation of Large Sections With Good Morphology

Previous work has shown that it is possible to fix entire amphibian lenses and cut thin equatorial sections that exhibit good morphological quality throughout the whole organ (Rae et al., 1983). To achieve this quality, however, the authors used strong fixation (10% formalin) and a lengthy embedding procedure. While this procedure resulted in excellent morphological preservation, it would preclude antibody labeling of proteins. Since understanding

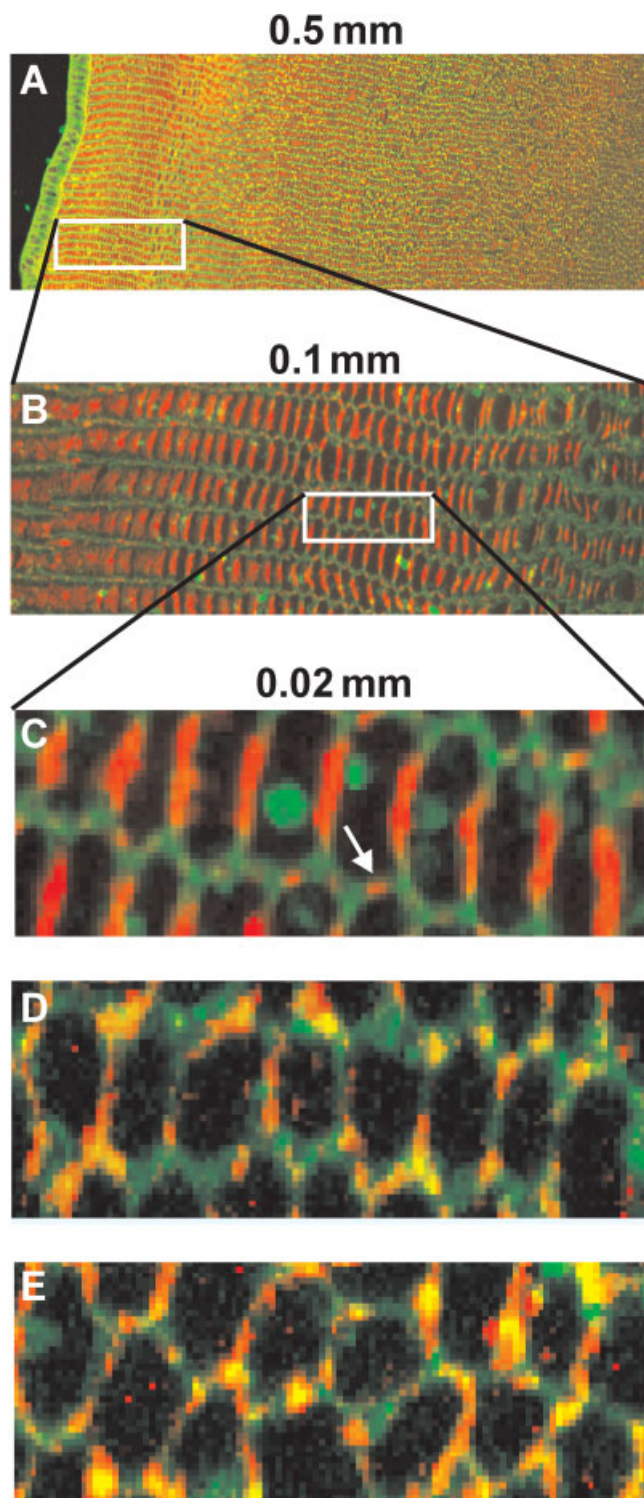


Fig. 4. Demonstration of the range of spatial scales encompassed by the composite image data. **A:** Overview taken from the equatorial lens radius in Fig. 3A, showing gross changes in cell morphology with increasing depth into the lens. **B:** Five-fold magnification of the boxed region in (A) showing local cell morphology. **C:** Five-fold magnification of the boxed region in (B) showing subcellular morphological detail. **D,E:** Data at the same magnification as in (C) but at distances of 500 and 700  $\mu\text{m}$  into the lens, respectively. Note that at this resolution the change in the expression pattern of labeled gap junctions (red) can be clearly identified. The arrow (C) indicates a small gap junction plaque on the narrow side of hexagonal fiber cells. The extent of the displayed data in the horizontal direction is indicated above each image. All images were extracted from the same original data. [Color figure can be viewed in the online issue, which is available at [www.interscience.wiley.com](http://www.interscience.wiley.com).]

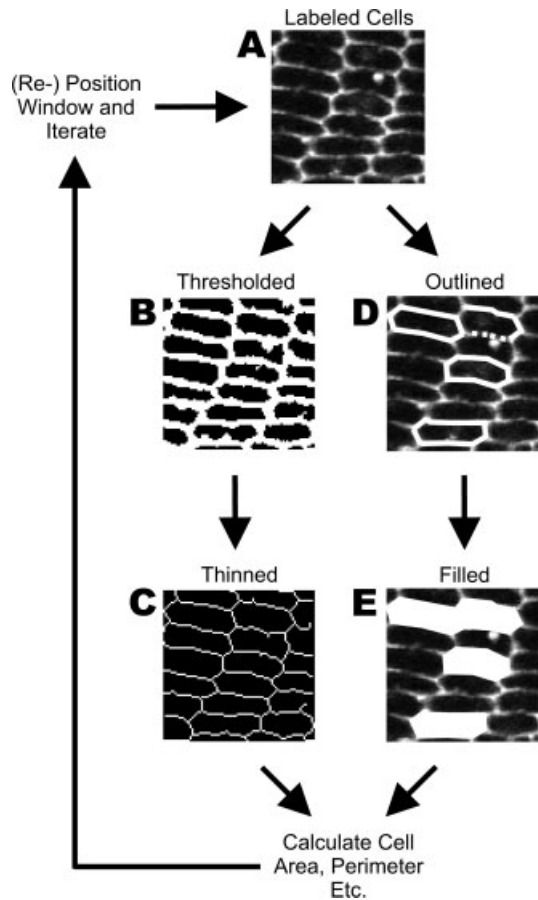


Fig. 5. Flow diagram of two algorithms for quantifying cell morphology. A small “window” (A) is positioned at one end of a large immunofluorescence image (e.g., Fig. 3A). Using the automated algorithm the signal within the window is thresholded to identify cell membranes (B) and then “thinned” to produce a membrane “skeleton” (C) from which cell areas and perimeters are obtained. Alternatively, cell outlines (D) are traced interactively and “filled” (E) to measure cell areas and perimeters. The window is then repositioned at specified intervals along the image and the calculations are repeated to produce a record of the changing morphology across the tissue.

the relationship between morphological structure and protein expression patterns requires good antibody labeling, it was necessary to develop a milder fixation protocol. The key to our protocol is to reduce fixative to a minimum to preserve antibody epitope while extending fixation time to allow the fixative to diffuse into the center of the lens. These two fixation variables are interrelated and our protocol reflects a compromise between morphological preservation and antibody labeling. Although significant time was required for the fixative to penetrate to the lens center, its morphology was similar to that reported in previous light microscopic studies using stronger fixation protocols (Bassnett, 1995; Rae et al., 1983). As shown in this study, our fixation protocol resulted in good preservation of Cx46 antibody epitopes and we have found that other lens proteins are also well preserved (Gonen et al., 2001).

### Combining High-Resolution Fluorescence Images

Studies of large-scale cytological variations in tissues by optical microscopy generally requires the investigator to choose between imaging small areas at high resolution or imaging large areas at low resolution. In our experience, typical microscopic fields of view require a sampling resolution of  $\sim 2000 \times 2000$  pixels. This follows from the Nyquist sampling theorem, which states that for a limited bandwidth signal with maximum spatial frequency  $f_{max}$  (here set by the optical resolution) the sampling frequency  $f_s$  must be greater than twice the maximum frequency  $f_{max}$  to avoid aliasing (which is effectively a source of noise). In other words, the field of view should be sampled at more than twice the optical resolution (determined by the numerical aperture) to achieve adequate sampling. Since tissue sections are usually larger than the field of view of high resolution objectives ( $NA > 1.0$ ), multiple fields of view must be combined in a seamless way. While the problem of creating such “photomosaics” is not a new one (e.g., Beck et al., 2000; Becker et al., 1996; Dani and Chaudhuri, 1995; Milgram, 1975; Ott, 1997), the specific challenge in our application was to overcome the problem of photobleaching to produce a composite image that was not only “seamless” to the eye but also appropriate for further automatic image analysis. In particular, the composite data should have no measurable discontinuities at the component image borders to avoid any analysis artifacts. To achieve this aim it was necessary to implement a beam suppression mechanism that avoided the bleaching problem illustrated in Figure 2 by ensuring that no area was subjected to the excitation laser beam, which was also not simultaneously imaged. In experimental systems where photobleaching is absent or irrelevant (or overscanning can be avoided by scanning sufficiently slowly), this feature should not be necessary (e.g., Becker et al., 1996). In many experimental contexts, however, a certain degree of photobleaching is unavoidable, especially when a variety of fluorescent markers of varying photostability is used to multilabel tissue sections. In connection with this point, it should be noted that a certain degree of “overscanning” is inevitable even with appropriate beam suppression when using conventional fluorescence imaging of thick sections. This problem resides in the cone of excitation extending beyond the image edges (see fig. 4 in Cannell and Soeller, 1997) which can be overcome by using TPM, which also avoids longitudinal chromatic aberration in multilabeled samples (Cannell and Soeller, 1997).

To achieve the accurate alignment of stacks to within pixel resolution, we used a cross-correlation approach (e.g., Dani and Chaudhuri, 1995; Ott, 1997). The advantage of this approach is the objective nature of the processing, which cannot be achieved by simply cropping, visually aligning images, and then “painting” to remove seams (Beck et al., 2000). While some authors have argued that correlation methods can be computationally costly and favored landmark-based techniques (Becker et al., 1996), modern computers are so fast that construction of cross-correlations of image boundaries is not limiting. In addition, by exploiting constraints derived from the precision of the stage control mecha-

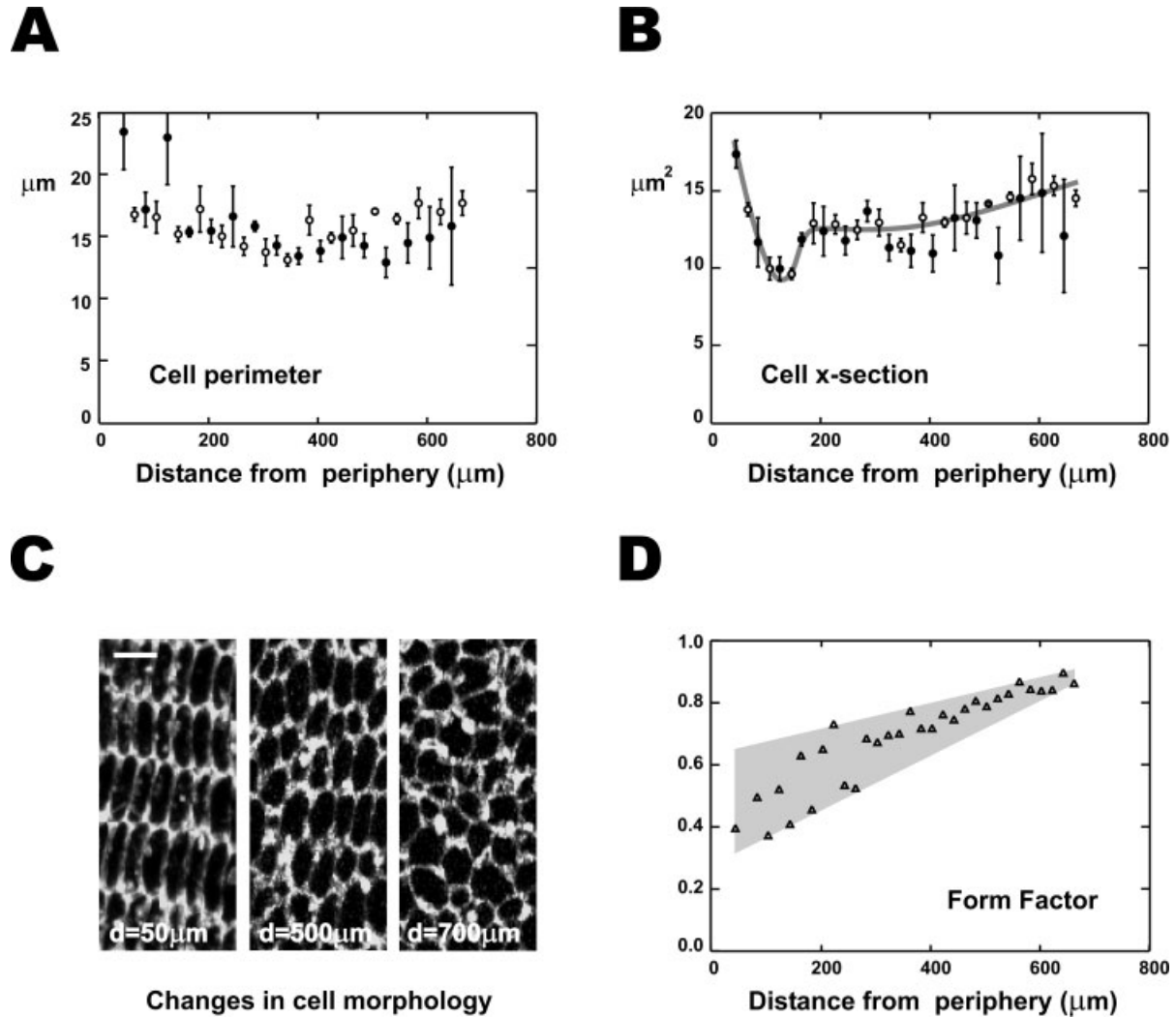


Fig. 6. Quantification of lens fiber cell morphology. **A,B**: Plots of cell perimeter and cross-sectional area using data from the image in Fig. 3A, collected by the automatic (hollow circles) and semiautomatic (filled circles) methods shown in Fig. 5. Both methods produced similar results. The curve in **B** was drawn by eye and shows the decrease

in cross-sectional area at a depth of 120  $\mu\text{m}$ . **C**: Images of cells at three distances  $d$  from the lens periphery, showing changing morphology. **D**: Plot of the “form factor,” an index of cell circularity. Cells become more circular with increasing depth into the lens. Scale bar = 5  $\mu\text{m}$ .

nism we greatly reduced the number of translational shifts that need to be explored. In the datasets shown here execution times were well below 1 second.

Since thin sections are essentially two-dimensional, it would be sufficient to perform the alignment and analysis in two dimensions only. However, the alignment method can be extended to three dimensions by computing 3D cross-correlations (while exploiting any constraints based on known stage and focus movements to minimize computational overhead). The utility of this approach is illustrated in Figure 3D. However, we would urge caution in applying quantitation when bleaching patterns are extended by the 3D nature of the specimen and conventional fluorescence imaging is used.

#### Image Processing and Morphological Analysis

The analysis of fiber cell perimeters and cross-sectional areas was performed with a fully automatic as

well as an operator-driven procedure. Both types of analysis agreed well, but the automatic approach was faster and resulted in measurements with lower statistical variation. The increased speed enabled much larger samples to be processed ( $>100$  cells per data point), which in turn increased the accuracy of the measurements. In addition, automated analysis does not suffer from operator bias.

The form factor measure  $FF$  is not particularly sensitive to errors in the determination of perimeter and cell area since these quantities are intimately linked. For example, for an elliptical cell shape, since the area of an ellipsoid is  $\pi ab$  and the perimeter is  $\sim\pi(1.5(a+b) - \sqrt{ab})$ ,  $FF = 16ab/(3a+3b-2\sqrt{ab})^2$  where  $a$  and  $b$  are the short and long axes, respectively. Using this formula,  $FF$  would have an error of  $\sim 10\%$  at  $a/b = 2$  ( $FF=0.8$ ) and  $\sim 17\%$  at  $a/b = 6$  ( $FF=0.4$ ) for a 10% error in  $a/b$ . Thus, for nearly circular cells the error in  $FF$  is approximately equal to the error(s) in  $a$  and  $b$  and

rises to 1.7 times the errors in  $a$  and  $b$  when the most elliptical cells are measured. Thus,  $FF$  is a reasonable indicator for changing cell ellipticity.

### Regional Differences in Fiber Cell Morphology

The structural changes observed are generally consistent with earlier developmental studies in the lens (e.g., Bassnett, 1995; al-Ghoul and Costello, 1997). Our results also agree with some quantitative results obtained by manual analysis of frog lens fiber cells using conventional light microscopy, scanning electron microscopy, and photography (Rae et al., 1983; Kuszak and Rae, 1982). Those studies also revealed a decrease in fiber cell cross-section in a narrow region near the lens periphery similar to the one we observed in the rat lens ( $\sim 120 \mu\text{m}$  from the periphery, see Fig. 6B). In the frog, this change was associated with the elongation of differentiating fiber cells (Kuszak and Rae, 1982). Inspection of our rat data shows that the reduction in cross-sectional area was due to a preferential decrease in fiber cell diameter in the radial direction compared to the circumferential direction.

In deeper regions of the rat lens, the fiber cell cross-section becomes progressively closer to a circle, a result unlike that of the frog, where fiber cells keep a flattened shape (aspect ratio  $> 3$ ) for more than 1 mm into the lens. Although the underlying cause of these differences is unknown, the ability of our methods to correlate protein expression and morphology over wide areas should help clarify which factors are responsible for these changes. Such studies will provide a powerful complement to the literature on fiber cell morphology and composition at the level of the electron microscope (see Kuszak, 1995; Zampighi et al., 2000). It is also possible that detailed knowledge of lens structure obtained in this way may help provide a structural foundation for the microcirculation model of the lens (Donaldson et al., 2001). More generally, our methods should be adaptable to other systems to help bridge the gap between knowledge of cell and tissue structure and the basis of tissue function.

### REFERENCES

- al-Ghoul KJ, Costello MJ. 1997. Light microscopic variation of fiber cell size, shape and ordering in the equatorial plane of bovine and human lenses. *Mol Vis* 3:2.
- Bassnett S. 1995. The fate of the Golgi apparatus and the endoplasmic reticulum during lens fiber cell differentiation. *Invest Ophthalmol Vis Sci* 36:1793–1803.
- Beck J, Murray J, Willows A, Cooper M. 2000. Computer-assisted visualizations of neural networks: expanding the field of view using seamless confocal montaging. *J Neurosci Methods* 98:155–163.
- Becker D, Ancin H, Szarowski D, Turner J, Roysam B. 1996. Automated 3-D montage synthesis from laser-scanning confocal images: Application to quantitative tissue-level cytological analysis. *Cytometry* 25:235–245.
- Bond J, Green C, Donaldson P, Kistler J. 1996. Liquefaction of cortical tissue in diabetic and galactosemic rat lenses defined by confocal laser scanning microscopy. *Invest Ophthalmol Vis Sci* 37:1557–1565.
- Cannell MB, Soeller C. 1997. High resolution imaging using confocal and two-photon molecular excitation microscopy. *Proc R Microsc Soc* 32:3–8.
- Dani P, Chaudhuri S. 1995. Automated assembling of images: image montage preparation. *Pattern Recogn* 28:431–445.
- Denk W, Piston D, Webb W. 1995. Two-photon molecular excitation in laser-scanning microscopy. In: Pawley J, editor. *Handbook of biological confocal microscopy*, 2nd ed. New York: Plenum Press.
- Donaldson P, Kistler J, Mathias R. 2001. Molecular solutions to mammalian lens transparency. *News Physiol Sci* 16:118–123.
- Gonen T, Grey AC, Jacobs MD, Donaldson PJ, Kistler J. 2001. MP20, the second most abundant lens membrane protein and member of the tetraspanin superfamily, joins the list of ligands of galectin-3. *BMC Cell Biol* 2:17.
- Gong X, Li E, Klier G, Huang Q, Wu Y, Lei H, Kumar N, Horwitz J, Gilula N. 1997. Disruption of alpha3 connexin gene leads to proteolysis and cataractogenesis in mice. *Cell* 91:833–843.
- Inoue S. 1995. Foundations of confocal scanned imaging in light microscopy. In: Pawley J, editor. *Handbook of biological confocal microscopy*, 2nd ed. New York: Plenum Press.
- Jacobs MD, Soeller C, Cannell MB, Donaldson PJ. 2001. Quantifying changes in gap junction structure as a function of lens fiber cell differentiation. *Cell Adhes Commun* 8:349–353.
- Kong T, Rosenfeld A. 1989. Digital topology: introduction and survey (image processing). *Comp Vis Graph Image Process* 48:357–393.
- Konig K. 2000. Multiphoton microscopy in life sciences. *J Microsc* 200:83–104.
- Kuszak J. 1995. The ultrastructure of epithelial and fiber cells in the crystalline lens. *Int Rev Cytol* 163:305–350.
- Kuszak J, Rae J. 1982. Scanning electron microscopy of the frog lens. *Exp Eye Res* 35:499–519.
- Lechleiter JD, Lin DT, Sieneart I. 2002. Multi-photon laser scanning microscopy using an acoustic optical deflector. *Biophys J* 83:2292–2299.
- Lichtstein D, Levy T, Deutsch J, Steinitz M, Zigler J, Russell P. 1999. The effects of digitalis-like compounds on rat lenses. *Invest Ophthalmol Vis Sci* 40:407–413.
- Milgram D. 1975. Computer methods for creating photomosaics. *IEEE Transact Comput* C-24:1113–1119.
- Ott SR. 1997. Acquisition of high-resolution digital images in video microscopy: automated image mosaicking on a desktop microcomputer. *Microsc Res Tech* 38:335–339.
- Rae J, Truitt K, Kuszak J. 1983. The use of procion dyes for light microscopy of the frog lens. *Invest Ophthalmol Vis Sci* 24:1167–1171.
- Russ J. 1995. *The image processing handbook*, 2nd ed. Boca Raton, FL: CRC Press.
- So PT, Dong CY, Masters BR, Berland KM. 2000. Two-photon excitation fluorescence microscopy. *Annu Rev Biomed Eng* 2:399–429.
- Soeller C, Cannell M. 1996. Construction of a two-photon microscope and optimisation of illumination pulse duration. *Pflugers Arch* 432:555–561.
- Soeller C, Cannell MB. 1999. Two-photon microscopy: imaging in scattering samples and three-dimensionally resolved flash photolysis. *Microsc Res Tech* 47:182–195.
- Wan H, Winton HL, Soeller C, Tovey ER, Gruenert DC, Thompson PJ, Stewart GA, Taylor GW, Garrod DR, Cannell MB, Robinson C. 1999. Der p 1 facilitates transepithelial allergen delivery by disruption of tight junctions. *J Clin Invest* 104:123–133.
- White T, Goodenough D, Paul D. 1998. Targeted ablation of connexin50 in mice results in microphthalmia and zonular pulverulent cataracts. *J Cell Biol* 143:815–825.
- Xu C, Zipfel W, Shear JB, Williams RM, Webb WW. 1996. Multiphoton fluorescence excitation: new spectral windows for biological nonlinear microscopy. *Proc Natl Acad Sci USA* 93:10763–10768.
- Young M, Tunstall M, Kistler J, Donaldson P. 2000. Blocking chloride channels in the rat lens: Localized changes in tissue hydration support the existence of a circulating chloride flux. *Invest Ophthalmol Vis Sci* 41:3049–3055.
- Zampighi G, Eskandari S, Kreman M. 2000. Epithelial organization of the mammalian lens. *Exp Eye Res* 71:415–435.